Yang *et al. Satellite Navigation* (2026) 7:4
https://doi.org/10.1186/s43020-026-00194-z

Satellite Navigation
https://satellite-navigation.springeropen.com/

ORIGINAL ARTICLE Open Access

Overbounding observation errors considering elevation-related distribution characteristics for maritime RT-PPP integrity monitoring

Fuxin Yang[1], Xiaobo Liu[1], Jie Zhang[1*], Weiyu Zhao[1], Liang Li[1] and Mohammed Quddus[2]

Abstract

Integrity monitoring ensures the reliability of Real-Time Precise Point Positioning (RT-PPP) by calculating the Protection Level (PL) in maritime applications. Overbounding the non-ideal observation errors for the PL plays a vital role in suppressing Misleading Information (MI) and improving system availability, including significant non-Gaussian errors such as multipath. The traditional two-step overbounding algorithm always uses a global overbounding coefficient with the largest value to envelop all non-ideal distribution of observation errors. The non-Gaussian errors, like multipath, can cause severe the non-ideal distortion of low-elevation-angle satellite observation errors, leading to the generation of larger overbounding coefficients. Furthermore, the PL can be constructed based on the traditional two-step overbounding algorithm in the position-domain to envelope Positioning Error (PE), and the MI can also be avoided. However, the constructed PL suffers from excessive conservation, and may reduce system availability. Therefore, a non-ideal observation error overbounding method considering elevation-related distribution characteristics is developed for maritime RT-PPP integrity monitoring. The method integrates the two-step overbounding algorithm to determine the differentiated overbounding coefficients related to different elevation intervals. Meanwhile, it is validated using two sets of real maritime experimental data in offshore and ocean areas. The results demonstrate that the developed method generates PL that more closely matches the PE The availability of the integrity monitoring system is improved by 16.18% and 11.88% for the two scenarios, respectively. The developed method can enhance the availability level of integrity monitoring. It can be applied to the dynamic positioning system of offshore vessels, thereby reducing the risks in precise operations.

Keywords Integrity monitoring, Two-step overbounding, Elevation, RT-PPP, Maritime

Introduction

Marine resource exploration, development and marine engineering construction rely on high-precision horizontal positioning solutions. Real-Time Precise Point Positioning (RT-PPP), with its advantages of no need of a base station and global coverage, can provide decimeter- to centimeter-level positional accuracy (Li et al., 2023; Long et al., 2023; Yang et al., 2019). Consequently, RT-PPP is a preferred technology for marine high-precision positioning services (Geng et al., 2010). Moreover, the International Maritime Organization (IMO) highlights

*Correspondence:
Jie Zhang
jiezhang@hrbeu.edu.cn
[1] College of Intelligent Systems Science and Engineering, Harbin Engineering University, Harbin 150001, China
[2] Centre for Transport Engineering and Modelling, Department of Civil and Environmental Engineering, Imperial College London, London SW2 2AZ, UK

© The Author(s) 2026. **Open Access** This article is licensed under a Creative Commons Attribution 4.0 International License, which permits use, sharing, adaptation, distribution and reproduction in any medium or format, as long as you give appropriate credit to the original author(s) and the source, provide a link to the Creative Commons licence, and indicate if changes were made. The images or other third party material in this article are included in the article's Creative Commons licence, unless indicated otherwise in a credit line to the material. If material is not included in the article's Creative Commons licence and your intended use is not permitted by statutory regulation or exceeds the permitted use, you will need to obtain permission directly from the copyright holder. To view a copy of this licence, visit http://creativecommons.org/licenses/by/4.0/.

that integrity is an essential criterion for maritime precision operations. Since IMO prioritizes horizontal integrity performance for RT-PPP, it specifies an Alert Limit (AL) of 2.5 m in the horizontal direction and an integrity risk requirement of $1 \times 10^{-5}/(3\,\mathrm{h})$ h for decimeter-level marine applications (IMO Resolution, 2002, 2004). Integrity monitoring of RT-PPP is essential to guarantee the reliability of high-precision positioning solutions. It involves promptly alerting users when system failures occur (Li et al., 2016). It thereby provides a safety boundary compliant with the standards for operations such as ship navigation and marine resource development.

Integrity monitoring always calculates an upper bound of Positioning Error (PE), named Protection Level (PL), to ensure the probability of the PL exceeding the AL is controlled within the integrity risk budget. Heßelbarth and Wanninger (2013) proposed an improved Receiver Autonomous Integrity Monitoring (RAIM) algorithm for dual-frequency Precise Point Positioning (PPP). This algorithm generates a 10 m horizontal PL. Therefore, it is unsuitable for high-precision position services due to conservative PL. To construct the upper bound of PE ranging from meter- to decimeter-level, a PPP integrity monitoring method was proposed, which is referred to the Multiple Hypothesis Solution Separation (MHSS) theory in aviation and the error models were established for aviation environments (Blanch et al., 2019; Gunning et al., 2018). Nevertheless, the error models in the aviation community are not applicable to maritime environment due to the more complex multipath effects. Wang et al. (2022) proposed a PPP integrity monitoring method utilizing the MHSS algorithm, which can provide decimeter-level PLs in open-sky areas. This method assumes that the measurement noise follows a Gaussian distribution. However, the PLs always fail to effectively envelop the PE, because the assumption of Gaussian-distributed observation errors does not fit actual errors. In this case, the PE will be larger than the PL, which leads to MI and seriously threatens marine safety–critical applications. Zhang et al. (2025) established a threat model for RT-PPP in marine precision operation environment. This method summarized potential risk sources, and classified the threat model of RT-PPP into hardware-mitigated, algorithm-mitigated, negligible, and non-negligible categories. Among them, non-Gaussian multipath and real-time product anomalies were identified as main non-negligible risks. To ensure the reliability of real-time precise satellite clock and orbit correction products, the real-time product interruptions and anomalies should be monitored. The data fusion method by multiple real-time products is adopted to handle the faults caused by single real-time product interruption (Chen et al., 2017; Mervart & Weber, 2011). The integrity monitoring methods in range-domain are widely proposed to detect anomalies in satellite clock and orbit corrections (Wang et al., 2025a, 2025b; Weinbach et al., 2018; Xiao et al., 2025; Zhang et al., 2024). Therefore, the integrity monitoring methods for system-side precise satellite clock and orbit correction products have been widely studied, and their reliability has been well ensured. Consequently, the non-ideal distribution characteristics of observation errors caused by marine multipath become the main risk source affecting the reliability of RT-PPP.

Multipath errors in maritime environments are stronger and non-Gaussian, primarily due to strong specular reflections from the flat sea surface, multiple reflections from vessel structures, and time-varying signal paths caused by vessel motion and sea state (He et al., 2018). The strength of multipath errors is closely related to satellite elevation angles: low-elevation signals are more susceptible to reflection, causing strong interference and larger errors, while higher elevation signals have less multipath effects as direct signals dominate and reflected energy decays. Therefore, modeling of multipath effects by elevation intervals better captures its statistical behavior and supports tighter error bounds for integrity monitoring.

To effectively prevent the MI caused by the severe multipath, overbounding methods have been widely applied in integrity monitoring methods. DeCleene (2000) proposed a symmetric unimodal Cumulative Distribution Function (CDF) overbounding method. However, this method only applies to symmetric unimodal distributions, but actual error distributions are neither symmetric nor unimodal (Blanch et al., 2018). Rife et al. (2006) proposed the Paired Bounding (PB), which allows arbitrary forms of error distribution. Blanch et al. (2018) proposed the two-step overbounding algorithm that combines the CDF overbounding with the PB algorithm, which can compute rigorous Gaussian overbounding distributions for any sample distribution. Zhang et al. (2025) compared the multipath Gaussian bounds between the PB and two-step overbounding algorithm for non-Gaussian multipath in marine environments. It was observed that the two-step overbounding method demonstrates a better fit to the actual error distribution compared to the PB method. Nevertheless, they do not account for the correlation between satellite elevation angles and multipath errors. A global overbounding coefficient with the largest value is determined to envelop all non-ideal distribution of multipath errors. Therefore, this reduces the availability of the integrity monitoring system. Liu and Jiang (2024) proposed the quantile overbounding method. They dynamically predict the overbounding standard deviation by using multi-sensor, thereby implementing

a differentiated overbounding strategy. It can better facilitate the bounding of the multipath error. However, this method is not applicable to the scenarios of single maritime GNSS users.

Multipath errors exhibit a clear correlation with satellite elevation angles. Specifically, as elevation angles increase, multipath errors generally decrease. This relationship renders dividing intervals by elevation angles a reasonable approach for multipath error analysis. Sirisha et al. (2019) investigated the statistical distribution of GNSS multipath error, taking into consideration different elevation angles ranging from 10° to 30°, 30° to 60° and 60° to 90°. However, this elevation angle range can lose important detailed information and fail to accurately capture the characteristics of multipath errors varying with elevation angles. Therefore, in this contribution, the two-step overbounding multipath error method is proposed considering elevation-related distribution characteristics. The calculated multipath errors are divided into 8 intervals with elevation angles from 10° to 90°, and the interval is 10° (Zhao et al., 2016). The selection of 10° as the interval width in this paper primarily follows the common practices in GNSS error modeling. In the field of GNSS error analysis and integrity monitoring, dividing elevation angles with a fixed interval is a widely adopted and empirically validated method. In the study on GBAS ionospheric anomaly monitoring, Zhao et al. (2016) explicitly stated that the original observation data were first "divided into 9 groups according to the elevation; each group contains 10 degrees" as part of their analytical procedure. This approach effectively captures the statistical variation characteristics of errors with elevation angles, while ensuring sufficient samples within each interval for reliable parameter statistics. Our method draws on this well-established concept and applies it to the overbounding modeling of multipath errors in maritime RT-PPP. It can effectively capture the distribution characteristics of multipath errors in different elevation angle intervals.

The differentiated overbounding coefficients are determined based on the two-step overbounding algorithm for different elevation angle intervals. Compared with the global overbounding cofficient, the overbounding gaussian distribution based on differentiated overbounding cofficients can better fit the actual errors distribution. Therefore, the proposed method overcomes the problem of overly conservative overbounding for the satellites with larger elevation angles using a global uniform overbounding coefficient. Second, the derived Probability of Hazardously Misleading Information (PHMI) of the proposed method is less than the actual PHMI requirement. It is proved that the proposed method can always meet the predefined integrity risk requirement. Third, the real offshore and ocean experiments are designed to validate the proposed method.

The organization of this paper is as follows: "MHSS-based RT-PPP integrity monitoring" section constructs the PL for RT-PPP based on MHSS; "Proposed method" section analyzes the multipath errors overbounding coefficients under different elevation intervals and verifies that the proposed method better fits the actual errors distribution compared with the uniform overbounding method; "Experimental results and discussions" section validates the performance of the proposed method in two maritime experiments; Finally, "Conclusions" section concludes the study.

Table 1 The RT-PPP processing strategy

Parameters	Processing strategy
Model	Dual-frequency IF combination
Cut-off elevation angle	10°
Ionospheric delay	Eliminated via IF combination
Tropospheric delay	Dry zenith delay: Calculated using saastamoinen model
	Wet zenith delay: estimated as parameters in EKF with random walk noise model 2.5×10^{-11} m/s
	Mapping function: GPT2w + GMF
Antenna phase center	Corrected by igs20.atx
Relativity effects, Earth rotation, site displacement effects	Corrected via empirical model
Satellite orbit and clock	Real-time precise clock and orbit correction products from IP: ppp-rtk.gipp.org.cn, Port: 2101
Parameter estimation method	Extended Kalman filter
IF ambiguities	Float solution, parameters estimated
Receiver position	Kinematic estimated as white noise (1×10^{-4})
Receiver clock	Parameters estimated

MHSS-based RT-PPP integrity monitoring

This section introduces the dual-frequency Ionospheric-Free (IF) combination PPP model and RT-PPP processing strategy. Then we construct the PL in the position-domain based on MHSS. The PL is constrained by both continuity risk and integrity risk. Finally, the influence of multipath errors on the PL is analyzed.

Real-time PPP model

The dual-frequency IF combination PPP eliminates the first-order ionospheric delay error, and the observation equations for pseudorange and carrier phase are as follows: (Zumberge et al., 1997):

$$\begin{cases} P_{\mathrm{IF}}^{(s)} = \dfrac{f_1^2 P_1^{(s)} - f_2^2 P_2^{(s)}}{f_1^2 - f_1^2} = \rho^{(s)} + \delta\rho^{(s)} + \mathrm{d}t_r + \mathrm{d}t^{(s)} + T_{\mathrm{trop}}^{(s)} + \varepsilon_{P_{\mathrm{IF}}^{(s)}} \\ \boldsymbol{\Phi}_{\mathrm{IF}}^{(s)} = \dfrac{f_1^2 \boldsymbol{\Phi}_1^{(s)} - f_2^2 \boldsymbol{\Phi}_2^{(s)}}{f_1^2 - f_1^2} = \rho^{(s)} + \delta\rho^{(s)} + \mathrm{d}t_r + \mathrm{d}t^{(s)} + T_{\mathrm{trop}}^{(s)} + N_{\mathrm{IF}}^{s} + \varepsilon_{\boldsymbol{\Phi}_{\mathrm{IF}}^{(s)}} \end{cases} \tag{1}$$

where f_1 and f_2 are the carrier phase frequencies; the superscript s stands for the satellite, and the subscript r for the receiver; $P_{\mathrm{IF}}^{(s)}$ and $\boldsymbol{\Phi}_{\mathrm{IF}}^{(s)}$ represent the pseudorange and carrier phase observations, respectively; $\rho^{(s)}$ stands for geometric distance between satellite and receiver, and $\delta\rho^{(s)}$ is the satellite orbit error; $\mathrm{d}t_r$ and $\mathrm{d}t^{(s)}$ denote the receiver and satellite clock errors; $T_{\mathrm{trop}}^{(s)}$ represents tropospheric delay error; N_{IF}^{s} represents the IF integer phase ambiguity; $\varepsilon_{P_{\mathrm{IF}}^{(s)}}$ and $\varepsilon_{\boldsymbol{\Phi}_{\mathrm{IF}}^{(s)}}$ represent the multipath and receiver noise for the IF pseudorange and carrier phase observations, respectively. Additionally, the corrections for phase wind-up (Wu et al., 1992), relativity effects (Ashby, 2003), tidal displacement, and earth rotation (Kouba, 2009) are applied using established empirical models.

In Eq. (1), the tropospheric error is separable into Zenith Hydrostatic Delay (ZHD) and smaller Zenith Wet Delay (ZWD). The ZHD can be modeled to millimeter accuracy, while the wet delay requires parameter estimation. (Bevis et al., 1992). Meanwhile, it utilizes real-time RTCM-SSR precise satellite orbit and clock correction products to enhance broadcast ephemeris, generating high-accuracy satellite orbit and clock. With real-time precise satellite orbit and clock correction products available, the pseudorange hardware delays for both satellites and receivers are absorbed by their respective clock error (Geng et al., 2022b). Carrier-phase hardware delays are assimilated within ambiguity parameters (Geng et al., 2022a). For residual errors that are difficult to model accurately, they are estimated as unknown parameters. The comprehensive processing strategy for maritime RT-PPP is summarized in Table 1. This provides a high-precision state estimation foundation for subsequent integrity monitoring method.

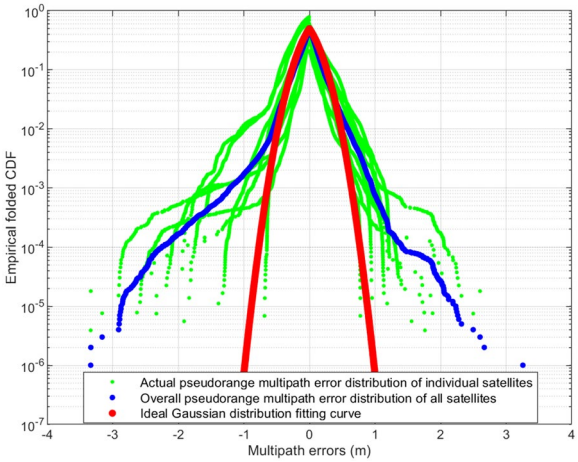


Fig.1 Empirical folded CDF plot of multipath errors

The stochastic model, a variance–covariance matrix $\mathbf{R}$, employs an elevation-dependent weighting function, expressed as,

$$\begin{cases} \mathbf{R} = \begin{pmatrix} \sigma_{\mathrm{SISE}}^2 + \sigma_{\mathrm{trop}}^2 + \sigma_P^2 & \sigma_{\mathrm{SISE}}^2 + \sigma_{\mathrm{trop}}^2 \\ \sigma_{\mathrm{SISE}}^2 + \sigma_{\mathrm{trop}}^2 & \sigma_{\mathrm{SISE}}^2 + \sigma_{\mathrm{trop}}^2 \end{pmatrix} \otimes \mathbf{I} \\ \sigma_{P/L}^2(\theta) = w_{\mathrm{type}}[a^2 + b^2/\sin(\theta)^2] \end{cases} \tag{2}$$

where σ_{SISE} is the standard deviation of signal-in-space ranging errors, which reflect the uncertainty in orbit and clock corrections; σ_{trop} is the standard deviation of the tropospheric delay; σ_P is the standard deviation of pseudorange measurement noise; σ_L is the standard deviation of carrier phase measurement noise; $\otimes$ is the Kronecker product operator; $\mathbf{I}$ is the identity matrix; θ is the elevation angle; a and b are typically empirical values; w_{type} is the weight factor for the type of satellites. For RT-PPP processing, the values of a and b are set to be the same, which are generally 0.003 m for carrier-phase measurements and 0.6 m for pseudorange measurements for BeiDou system, and 0.003 m for carrier-phase measurements and 0.3 m for pseudorange measurements for GPS system. w_{type} is set to 1.0 for GPS satellites, BeiDou inclined geosynchronous orbit and medium orbit satellites and 100.0 for BeiDou geostationary orbit satellites.

The overbounding coefficient f_h can be calculated based on the proposed Overbounding algorithm. Subsequently, f_h can be applied to the standard deviation of the measurement noise $\sigma_{P/L}$.

PL for RT-PPP integrity monitoring

Since IMO prioritizes horizontal integrity performance for RT-PPP, integrity monitoring uses the Horizontal Protection Level (HPL) as an upper bound of the Horizontal Positioning Error (HPE). To derive rigorous error bounds

and achieve robust integrity, constraints must be applied to potential fault modes at the user end. Therefore, the MHSS method is adopted for RT-PPP integrity monitoring, which isolated and assesses multiple fault hypotheses to enhance the integrity. Given the specific demands of maritime precision applications, particular emphasis is placed on horizontal protection performance. Within the MHSS framework, the HPL for each fault subset is constructed by jointly bounding integrity risk and continuity risk, accounting for the impact of all hypothesized fault modes,

$$H_{\mathrm{HPL}} = \max\left[Q^{-1}\left(\frac{P_{\mathrm{cont},i}}{N-1}\right)\sigma_{ss}^{(i)} + Q^{-1}\left(\frac{P_{\mathrm{IR},i}}{NP(H_i)}\right)\sigma^{(i)}\right] \tag{3}$$

where H_{HPL} represents the HPL at the current epoch; $\sigma_{ss}^{(i)}$ represents the standard deviation of the horizontal position error between the all-in-view solution and fault subset i; $P(H_i)$ is the prior probability of fault mode; $\sigma^{(i)}$ is the standard variance of HPE under the fault subset I; N is the number of satellites at the current epoch; Q^{-1} is the inverse function of the normal distribution; $P_{\mathrm{IR},i}$ represents the integrity risk, and $P_{\mathrm{cont},i}$ indicate the continuity risk.

The horizontal positioning error variance σ_H and the observation error variance σ are linked with the Horizontal Dilution of Precision (HDOP). Based on the construction of the HPL in Eq. (3), its assumption is built on the observation errors following a Gaussian distribution. Each observation error is mapped to the positioning domain through convolution, such that the positioning errors also follow a Gaussian distribution. However, significant unmodeled errors such as multipath cause the non-Gaussian characteristics of the observation errors. This may lead to uncertainties in the construction of the HPL (Zhang et al., 2022). Therefore, compensation for non-Gaussian errors is essential to ensure the Gaussian distribution premise.

Proposed method

To suppress MI and improve system availability, this section establishes a Gaussian overbounding framework in range-domain based on a two-step overbounding algorithm, especially the differentiated overbounding coefficients are determined related to different elevation angles intervals, and the flow chart of proposed method for RT-PPP is given. Moreover, integrity assessment is given to satisfy the predefined integrity risk requirement.

The two-step overbounding algorithm

Significant unmodeled errors such as multipath make the observation errors exhibit non-Gaussian characteristics. This may lead to uncertainties in the construction of the PL. A dataset of the GPS/BeiDou observations was collected at ststion JENG on November 15, 2024, with a sampling rate of 30 s. Subsequently, the pseudorange multipath errors were extracted using the method proposed by Seepersad, (2015). The distribution of pseudorange multipath errors is shown in Fig. 1. It can be concluded that the multipath errors exhibit obviously non-Gaussian distribution characteristic.

Once the multipath errors of dual-frequency IF pseudorange observation were extracted, the actual multipath errors distribution $G_{\mathrm{a}}(x)$ can be obtained. The overbounding coefficients can be determined based on the two-step overbounding algorithm. It first defines two overbounding distributions: one for the left side and the other for the right side (Blanch et al., 2018). Since the processing steps for the two overbounding distributions are identical, the procedure based on the left-side overbounding is described as follows:

$$\begin{cases} \mathrm{Step1}: G_{\mathrm{su}}(x) \geq G_{\mathrm{a}}(x), \forall x \\ \mathrm{Step2}: G_{\mathrm{ob}}(x) \geq G_{\mathrm{su}}(x), \forall x \leq 0 \end{cases} \tag{4}$$

where G denotes the CDF.G_{a} represents actual multipath errors distribution, G_{su} denotes a unimodal symmetric distribution, G_{ob} represents the Gussian bound of G_{su}, and x denotes the observation errors.

The process consists of two steps: first, the actual error distribution $G_{\mathrm{a}}(x)$ is converted into a unimodal symmetric distribution $G_{\mathrm{su}}(x)$; second, this distribution is used to establish a Gaussian overbound $G_{\mathrm{ob}}(x)$. The process for the right-side overbounding distribution is consistent with that of the left-side. It only requires $G_{\mathrm{su}}(x)$ adjusting to $G_{\mathrm{su}}(-x)$ for processing.

The overbounding coefficient is calculated via the two-step overbounding algorithm, which is defined as the ratio of the overbounding standard deviation σ_{o} to the actual multipath error standard deviation σ, expressed as:

$$\begin{cases} f = \dfrac{\sigma_{\mathrm{o}}}{\sigma} \\ \sigma_{\mathrm{o}} = \max\left(\sigma_L, \sigma_R\right) \end{cases} \tag{5}$$

where σ_L is the standard deviation of the Gaussian overbounding for the left-side CDF, σ_R is the standard deviation of the Gaussian overbounding for the right-side CDF, and σ represents the Gaussian fitted standard deviation calculated by the actual multipath errors distribution $G_{\mathrm{a}}(x)$.

The Gaussian overbounding of position-domain errors is obtained by enveloping non-Gaussian multipath errors using the two-step overbounding algorithm. To maintain the balance of noise magnitude differences between pseudorange and carrier phase, the standard deviations are inflated by the same multiple as follows.

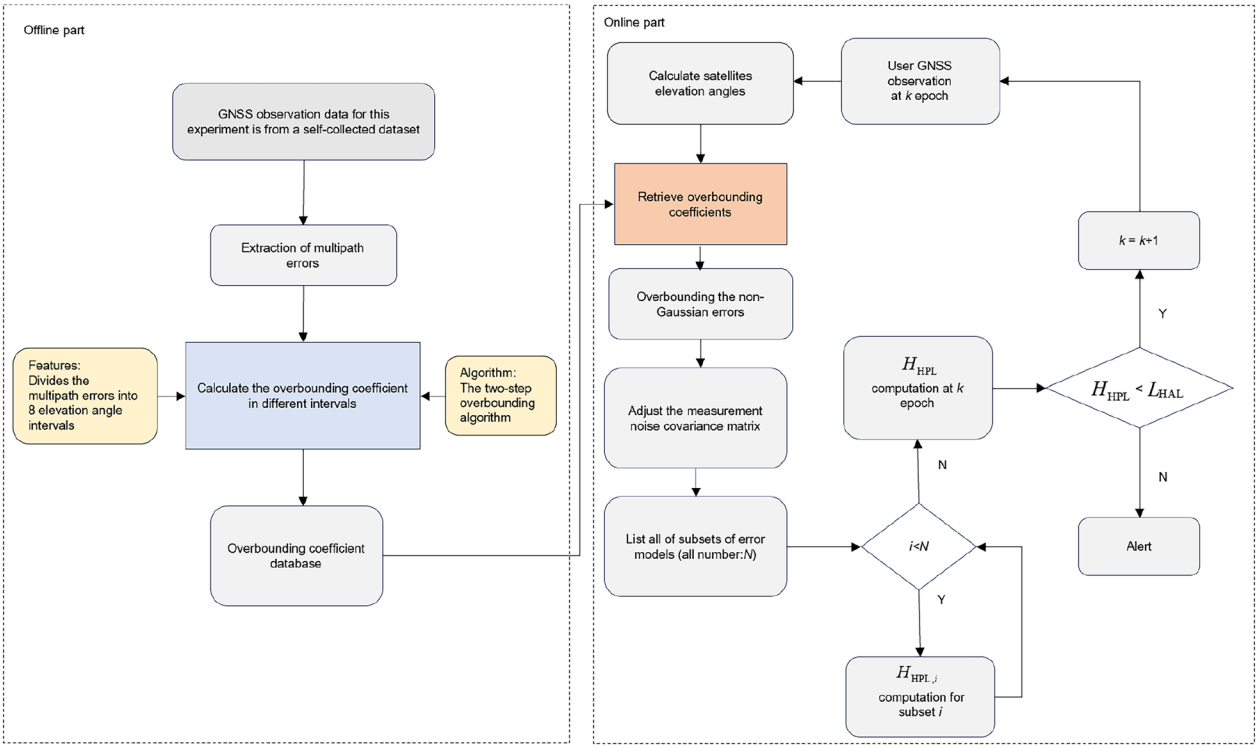


Fig.2 The flow chart of the proposed method

$$\begin{cases} \sigma_{o,P} = f\sigma_P \\ \sigma_{o,L} = f\sigma_L \end{cases} \tag{6}$$

where σ_P and σ_L represent the multipath errors of pseudorange and carrier phase, respectively. f is calculated according to Eq. (5).

The conventional two-step overbounding algorithm compensates for the non-Gaussian distribution of the multipath errors by calculating a specific overbounding coefficient. This coefficient ensures that the overbounding distribution envelopes all reasonable error distributions to guarantee that the HPL constructed in the position-domain can envelope the HPE and avoid the MI.

Determination of elevation-related overbounding coefficient

Multipath errors are highly correlated with the satellite elevation angles. Therefore, the multipath errors are partitioned into 8 intervals according to elevation angles, and the overbounding coefficient for each elevation interval is calculated. The actual multipath errors x are divided into 8 intervals $\theta_h \in ([10°, 20°)\ [20°, 30°)...[70°, 80°)\ [80°, 90°))$. For each elevation interval θ_h,

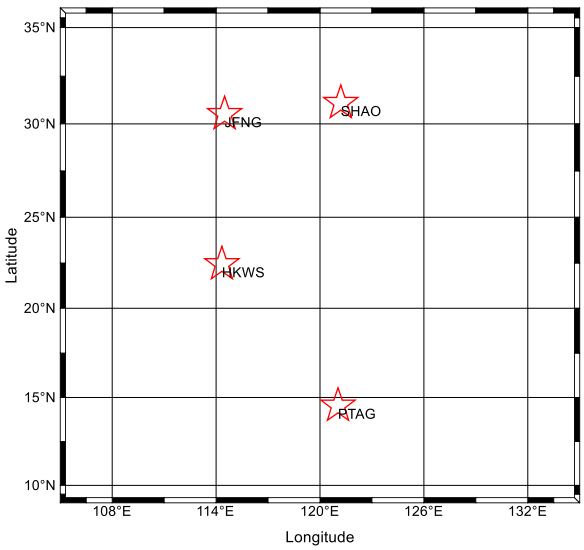


Fig.3 Distribution of IGS stations

$$\begin{cases} \sigma_{L,h} = \min\left[\sigma | G_{ob}(x_h) \geq G_{su}(x_h) \geq G_a(x_h), \forall x_h \leq 0\right] \\ \sigma_{R,h} = \min\left[\sigma | G_{ob}(x_h) \geq G_{su}(x_h) \geq G_a(x_h), \forall x_h > 0\right] \end{cases} \tag{7}$$

Based on the value range of the variable x_h, Eq. (7) divides σ into two categories, $\sigma_{L,h}$ and $\sigma_{R,h}$, for solution. Both of

Table 2 Detailed descriptions of three methods

Integrity monitoring method name	Method description
Integrity-A	Without overbounding method
Integrity-B	The two-step overbounding with a largest global overbounding coefficient
Integrity-C	The two-step overbounding with differentiated overbounding coefficients related to elevation angles (the proposed method)

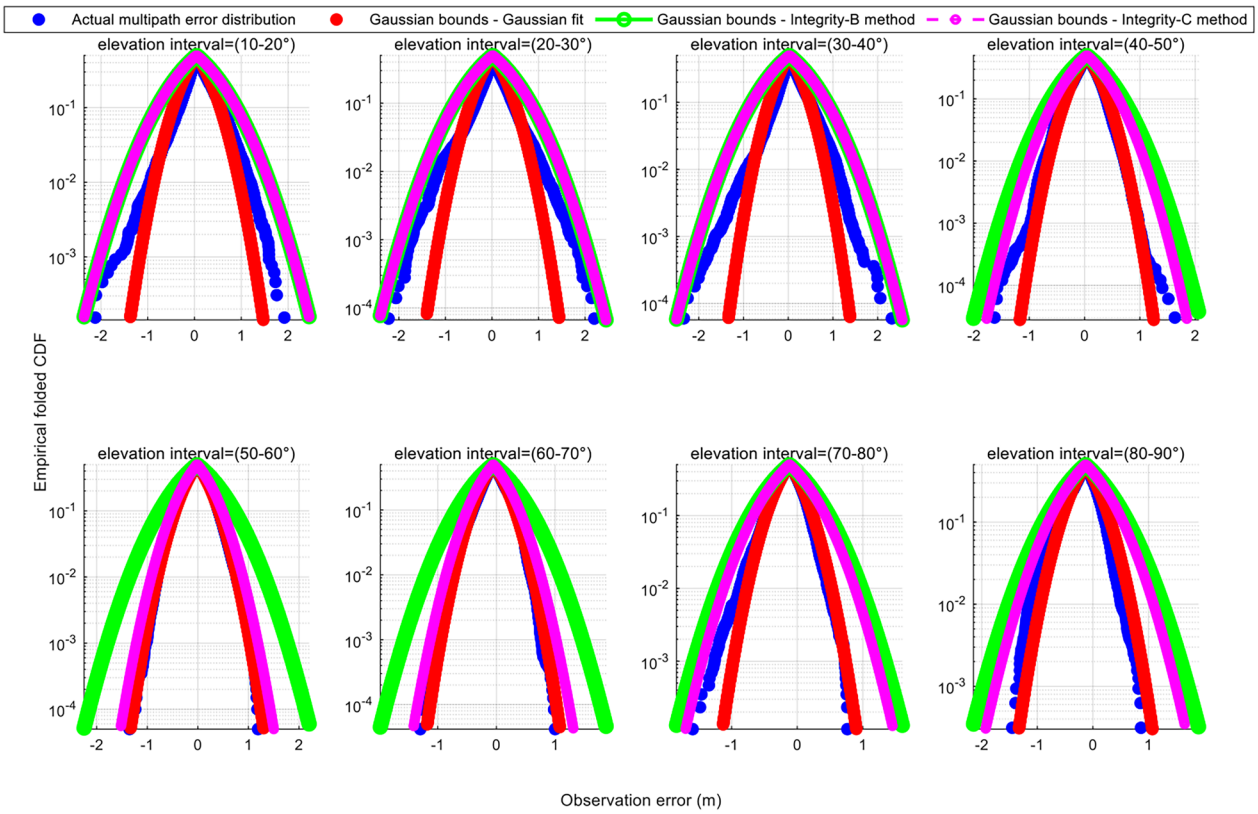


Fig.4 The overbounding effect of the Integrity-A, Integrity-B, and Integrity-C on the actual errors for different elevation intervals

them are the minimum σ values that satisfy the constraint condition $G_{\mathrm{ob}}(x_h) \geq G_{\mathrm{su}}(x_h) \geq G_{\mathrm{a}}(x_h)$. Equation (7) shows that overbounding sigma $\sigma_{L,h}$ and $\sigma_{R,h}$ for both the right and left envelopes are determined by the two-step overbounding algorithm in the elevation interval θ_h.

The Gaussian constraint for multipath error is defined by evaluating both the left and right envelopes and choosing the larger value.

$$\sigma_h = \max\left(\sigma_{L,h}, \sigma_{R,h}\right) \tag{8}$$

Then, the multipath errors overbounding coefficient f_h can be determined based on the two-step overbounding algorithm as follows:

$$f_h = \frac{\sigma_h}{\sigma_m} \tag{9}$$

where σ_m represents the Gaussian fitted standard deviation calculated by the actual multipath error distribution in the elevation interval θ_h.

The specific mathematical relationship between the overbounding coefficient and HPL can be established

Table 3 Comparison of overbounding coefficients

Station name	Integrity-B overbounding coefficient	Integrity-C overbounding coefficients in different elevation intervals							
		Elevation intervals 10–20°	Elevation intervals 20–30°	Elevation intervals 30–40°	Elevation intervals 40–50°	Elevation intervals 50–60°	Elevation intervals 60–70°	Elevation intervals 70–80°	Elevation intervals 80–90°
HKWS	1.78	1.78	1.78	1.78	1.6	1.55	1.5	1.2	1.15
SHAO	1.7	1.7	1.7	1.7	1.62	1.5	1.5	1.3	1.2
JFNG	1.8	1.8	1.8	1.8	1.7	1.65	1.6	1.4	1.3
PTAG	1.75	1.75	1.75	1.75	1.6	1.6	1.45	1.3	1.3

with the overbounding algorithm. This algorithm proves that after convolution, the envelope boundaries of a set of observation errors under the assumption of mutual independence can still form the envelope boundary of positioning errors in the position domain. Detailed assessment procedures can be found in the referenced literature (Blanch et al., 2018; Rife et al., 2006).

Specifically, after overbounding, the multipath errors form an envelope boundary f_h in the range domain, i.e.,:

$$\int_{-\infty}^{x} f(t)\mathrm{d}t \le \int_{-\infty}^{x} f_h(t)\mathrm{d}t, \forall x \le 0 \tag{10}$$

Therefore, after convolution of the corresponding range errors of different satellites, the following relationship holds in the position domain:

$$\int_{-\infty}^{x} (f * g)(t)\mathrm{d}t \le \int_{-\infty}^{x} (f_o * g)(t)\mathrm{d}t, \forall x \le 0 \tag{11}$$

where, $f * g$ denotes the convolution of different range errors, and g represents another range error.

Using the above equation, the envelope boundary of positioning errors in the position domain can be derived, and thus the standard deviation of positioning errors considering multipath expansion, denoted as σ_o, can be obtained. Since the formula of HPL is constructed based on the statistical characteristics of positioning errors, to establish the direct relationship between the two, the expression of HPL considering multipath overbounding is as follows:

$$H_{\mathrm{HPL}} = \max\left[Q^{-1}\left(\frac{P_{\mathrm{cont},i}}{N-1}\right)\sigma_{ss,o}^{(i)} + Q^{-1}\left(\frac{P_{\mathrm{IR},i}}{NP(H_i)}\right)\sigma_o^{(i)}\right] \tag{12}$$

Figure 2 illustrates the framework of the proposed method. The observation dataset used in the offline phase of this flow chart is derived entirely from the GNSS observation data in the same experiment. For a specific voyage experiment, raw GNSS observation data collected in the experiment are designated as the observation dataset. Both the calculation of overbounding coefficients and the subsequent positioning analysis are performed based on this experimental dataset. In the offline phase, the GNSS observation data collected in this experiment are utilized to extract multipath errors and calculate the overbounding coefficients for each elevation angle interval in post processing. Then, the overbounding coefficients are determined for each interval based on the two-step overbounding algorithm and stored in the dataset. In the online phase, the user obtains real-time GNSS observations at the current epoch, computes the elevation angles of visible satellites, and retrieves the corresponding overbounding coefficients from the database. These coefficients are used to inflate the non-Gaussian multipath errors according to elevation angles and adjust the measurement noise covariance matrix. Subsequently, based on the MHSS, the final HPL (H_{HPL}) is determined by synthesizing the sub-protection levels corresponding to all fault subsets. L_{HAL} represents the AL in the horizontal direction. If $H_{\mathrm{HPL}} \ge L_{\mathrm{HAL}}$, this indicates a test failure, and an alert needs to be issued to the user. If $H_{\mathrm{HPL}} < L_{\mathrm{HAL}}$, this signifies a test pass, meaning the receiver has passed the integrity monitoring check and proceeds to the next epoch.

To verify that the proposed method better fits the actual errors distribution, the GPS/BDS observation data at static IGS stations were collected over 3 days with a sampling interval of 30s. HKWS, SHAO, and PTAG are coastal stations, and JFNG is an inland station. Figure 3 shows the distribution of these stations. Furthermore, the multipath errors are extracted for dual-frequency IF pseudorange observation, and the comparisons were made among the traditional two-step overbounding method with a largest global overbounding coefficients, the proposed method with differentiated overbounding coefficients, and the method without overbounding. The details of the three methods are described in Table 2.

Figure 4 represents the non-Gaussian overbounding effect of the Integrity-A, Integrity-B and Integrity-C on the actual errors for different elevation angle interval, respectively. Taking the station HKWS as an example, the extracted multipath errors are partitioned into 8 intervals from 10° to 90° with10°. The bule dots represent the actual errors distribution. The red dots, green dots, and pink dots respectively represent the Gaussian

Table 4 The values of key integrity parameters

Items	Value
Horizontal AL (L_{HAL})	2.5 m
Integrity risk ($P_{IR,i}$)	1×10^{-5}/(3 h)
Continuity risk ($P_{cont,i}$)	1×10^{-6}
Prior failure probability	3.3×10^{-4}



Fig.5 Maritime vessel movement trajectory

bounds by integrity-A, integrity-B, and integrity-C. Note that the actual errors exhibit non-Gaussian characteristics and Integrity-A is the Gaussian fit of the actual errors. Integrity-B with the largest global overbounding coefficient can effectively envelope the actual error at low elevation angles. But for the satellites with high elevation angles, the overbounding model is overly conservative. Integrity-C selects differentiated overbounding coefficients for different elevation angle intervals. Therefore, the overbounding model can better fit the actual errors. The overbounding cofficients for integrity-B and integrity-C are given in Table 3.

Table 3 shows that the overbounding coefficients of integrity-B and integrity-C remain consistent between 10° and 40°; For the elevation angles greater than 40°, the overbounding coefficients gradually decrease with increasing elevation angles. Taking the station HKWS as an example, compared with Integrity-B, Integrity-C reduces the overbounding coefficients by 10.1%, 12.9%, 15.7%, 32.8%, and 35.4% in the five elevation intervals above 40°, respectively. The overbounding coefficients calculated by Integrity-B are overly conservative, though they effectively envelope multipath errors. The Integrity-C calculates elevation angle-dependent overbounding coefficients for different intervals. It better fits actual multipath errors to establish more realistic Gaussian bounds. Note that the Integrity-A method without overbounding, it is not shown in Table 3.

Table 5 Receiver system configuration for the offshore experiment

Items	Value/Type
Data type	BDS (B1I/B3I
	GPS (L1/L2)
Sampling time	00:53 to 02:52 on March 14, 2024, (UTC)
Sampling frequency	1 Hz
Receiver type	MA-NP 0101
Antenna type	HX-CSX601A

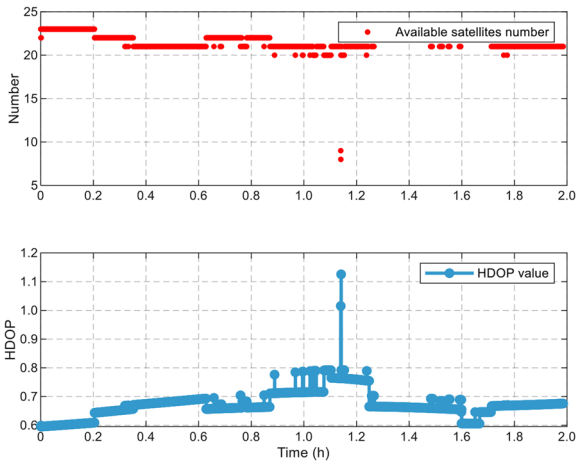


Fig.6 The available satellite number and HDOP value

Integrity assessment

The Probability of Hazardously Misleading Information (PHMI) is a core metric for integrity monitoring, defined as the probability that the HPE exceeds both the HPL and the AL. To protect integrity, the PHMI with Integrity-C must be less than the actual PHMI requirement. In this paper, the HPL in the RT-PPP integrity monitoring algorithm is constructed based on the MHSS theory. Therefore, the actual integrity risk shall be constrained within the integrity risk budget indices, which are expressed as:

$$\begin{aligned} P_{PHMI,A} &= \sum_{i=0}^{N-1} \left(P(\left| \Delta x^i \right| \geq H_{HPL,i} | i \right|) P_{ap,i} \Big) \\ &\leq \sum_{i=0}^{N-1} \left(P_{PHMI,i} \right) \\ &= P_{PHMI,req} \end{aligned} \tag{13}$$

where Δx^i denotes the horizontal positioning error of fault subset i, N is the number of fault subsets, and $P_{\mathrm{PHMI,req}}$ represents the integrity risk budget index, also known as the PHMI, which can be allocated to each fault

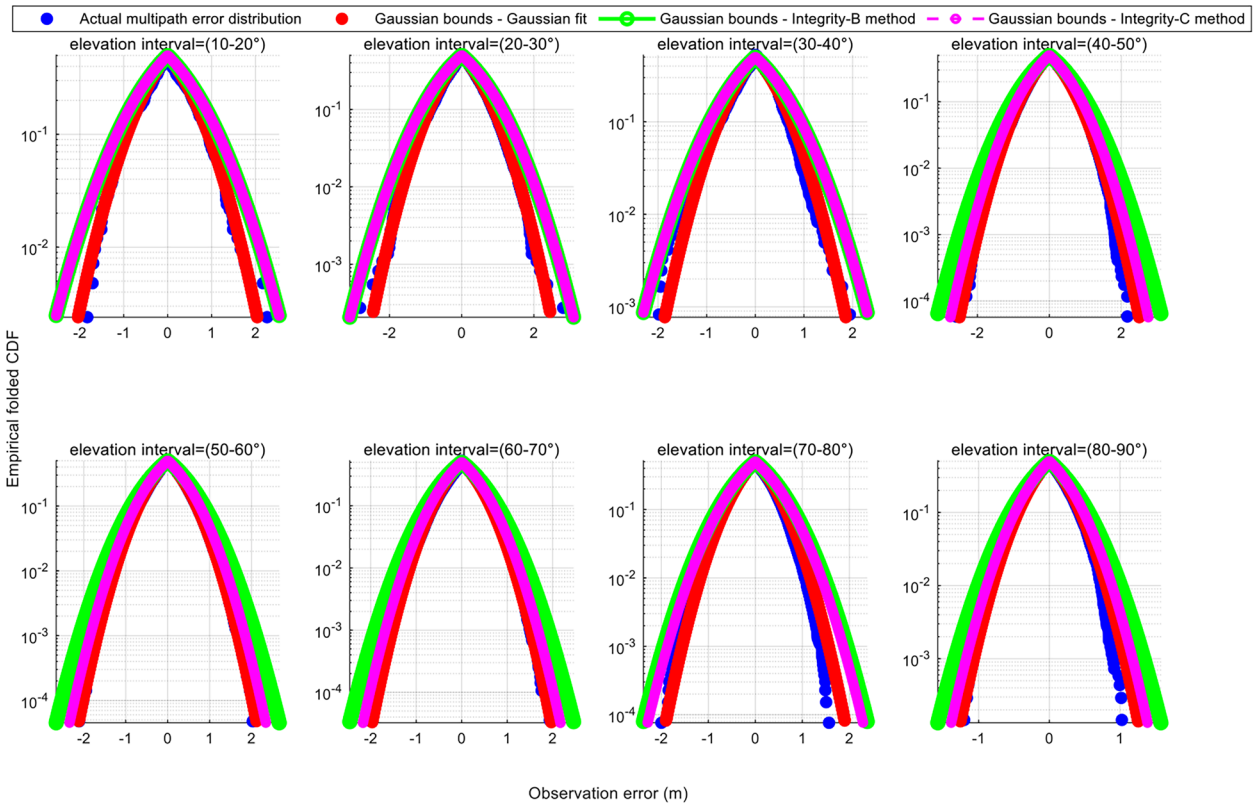


Fig.7 Gaussian bounds of multipath errors based on elevation intervals

Table 6 Comparison of overbounding coefficients

Integrity-B overbounding coefficient	Integrity-C overbounding coefficients in different elevation intervals							
	Elevation intervals 10–20°	Elevation intervals 20–30°	Elevation intervals 30–40°	Elevation intervals 40–50°	Elevation intervals 50–60°	Elevation intervals 60–70°	Elevation intervals 70–80°	Elevation intervals 80–90°
1.25	1.25	1.25	1.25	1.20	1.20	1.20	1.10	1.10

subset i, i.e., $P_{\mathrm{PHMI},i}$. $P_{\mathrm{PHMI,A}}$ denotes the original integrity risk corresponding to the RT-PPP integrity monitoring algorithm.

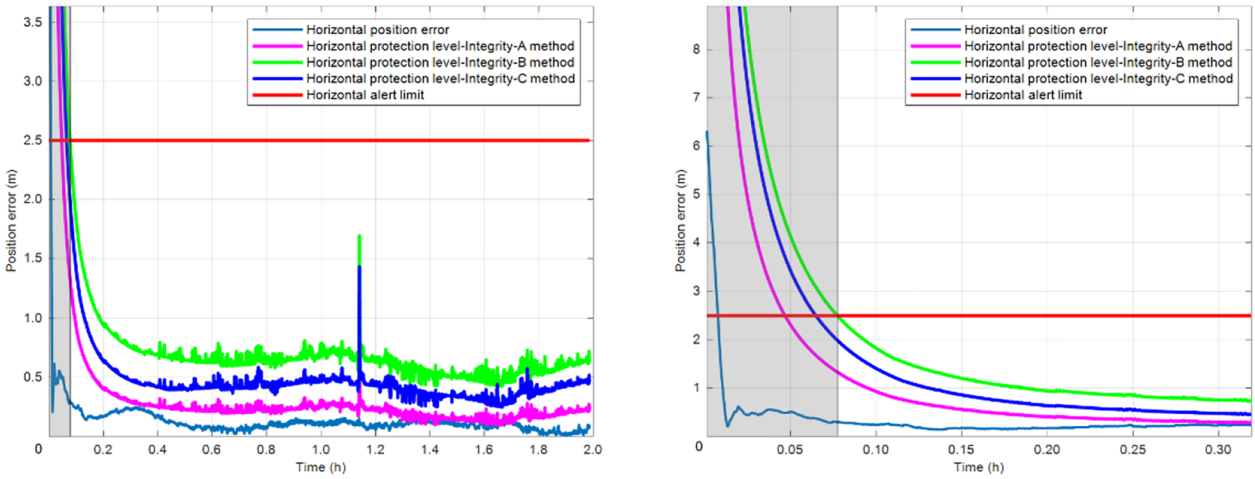
From previous section, the proposed Integrity-C method can compensate for the impact of distortions caused by non-Gaussian errors such as multipath, and its overbounding coefficient is more optimal than that of the Integrity-B method. Therefore, the HPL constructed based on the Integrity-C method has the following relationship:

$$H_{\mathrm{HPL},i} \le H_{\mathrm{HPL,C},i} \le H_{\mathrm{HPL,B},i} \tag{14}$$

where $H_{\mathrm{HPL,C},i}$ denotes the HPL under fault mode i constructed based on the Integrity-C algorithm, $H_{\mathrm{HPL,B},i}$ represents the HPL based on the Integrity-B method, and $H_{\mathrm{HPL},i}$ is the original HPL without overbounding processing.

Based on the HPL constructed by different algorithms, the corresponding integrity risks are as follows:

$$\begin{cases} \sum_{i=0}^{N-1} \left(P\left(\left| \Delta x^i \right| \ge H_{\mathrm{HPL},i} | i \right) P_{ap,i} \right) = P_{\mathrm{PHMI,A}} \\ \sum_{i=0}^{N-1} \left(P\left(\left| \Delta x^i \right| \ge H_{\mathrm{HPL,C},i} | i \right) P_{ap,i} \right) = P_{\mathrm{PHMI,C}} \\ \sum_{i=0}^{N-1} \left(P\left(\left| \Delta x^i \right| \ge H_{\mathrm{HPL,B},i} | i \right) P_{ap,i} \right) = P_{\mathrm{PHMI,B}} \end{cases} \tag{15}$$



a The HPL of three integrity monitoring methods **b** A detailed view of the initial convergence phase from

Fig. 8 The HPL of three integrity monitoring methods in offshore experiment

where $P_{\mathrm{PHMI,C}}$ denotes the integrity risk corresponding to the Integrity-C method, and $P_{\mathrm{PHMI,B}}$ represents the integrity risk of the Integrity-B method.

Therefore, we can derive the relationships among the different integrity risks as follows by combining Eq. (13) and Eq. (14):

$$P_{\mathrm{PHMI,B}} \leq P_{\mathrm{PHMI,C}} \leq P_{\mathrm{PHMI,A}} \leq P_{\mathrm{PHMI,req}} \tag{16}$$

It can be concluded that the integrity risks corresponding to the HPL processed by overbounding are all less than the actual integrity risk budget indices, without introducing additional integrity risk to the system, thus satisfying the system integrity requirements. Furthermore, from Eq. (16) the integrity risk with the Integrity-B method is more conservative compared with the Integrity-C method based on the elevation-related distribution characteristics. This demonstrates the effectiveness of the proposed method, which achieves higher availability while meeting integrity.

Experimental results and discussions

To fully evaluate the proposed method in maritime RT-PPP, the performances including MI, the ratio of HPL to HPE, and availability are compared with Integrity-A, Integrity-B and Integrity-C. The HPE is the difference between the RT-PPP position solutions and the reference values, which refers to the position error in the horizontal direction. In this study, the variable E_{HPE} is used to represent HPE. Note that availability is defined as the state that $H_{\mathrm{HPL}} < L_{\mathrm{HAL}}$ and $E_{\mathrm{HPE}} < L_{\mathrm{HAL}}$. MI is defined as $H_{\mathrm{HPL}} < E_{\mathrm{HPE}}$. The $R_{H_{\mathrm{HPL}}/E_{\mathrm{HPE}}}$ is defined as the ratio of HPL to HPE. A smaller ratio indicates that the HPL is closer to the actual HPE, reflecting a less conservative bound and thus a higher sensitivity to potential faults. This metric aligns with the goal of integrity monitoring: to provide a safe yet non-excessive error bound. Furthermore, two experiments on offshore and open sea (approximately 200 km from the coastline) were conducted. Integrity-related parameters in the experiments refer to the requirements of IMO (IMO Resolution, 2004) as shown in Table 4.

Offshore experiment

An offshore dynamic experiment was conducted from 00:53 to 02:52 on March 14, 2024 (UTC). The starting point is (35°88 N, 120°07 E), and the ending point is (35°81 N,120°12 E). The position reference (centimeter-level accuracy) is obtained via RTK fixed solutions, with the maximum distance between the base station and the

Table 7 Performance statistics with different methods

Integrity monitoring method	Horizontal protection level (95%)	$R_{H_{\mathrm{HPL}}/E_{\mathrm{HPE}}}$
MHSS-based integrity monitoring with Integrity-A	0.653	2.650
MHSS-based integrity monitoring with Integrity-B	1.553	6.313
MHSS-based integrity monitoring with Integrity-C	1.237	5.022

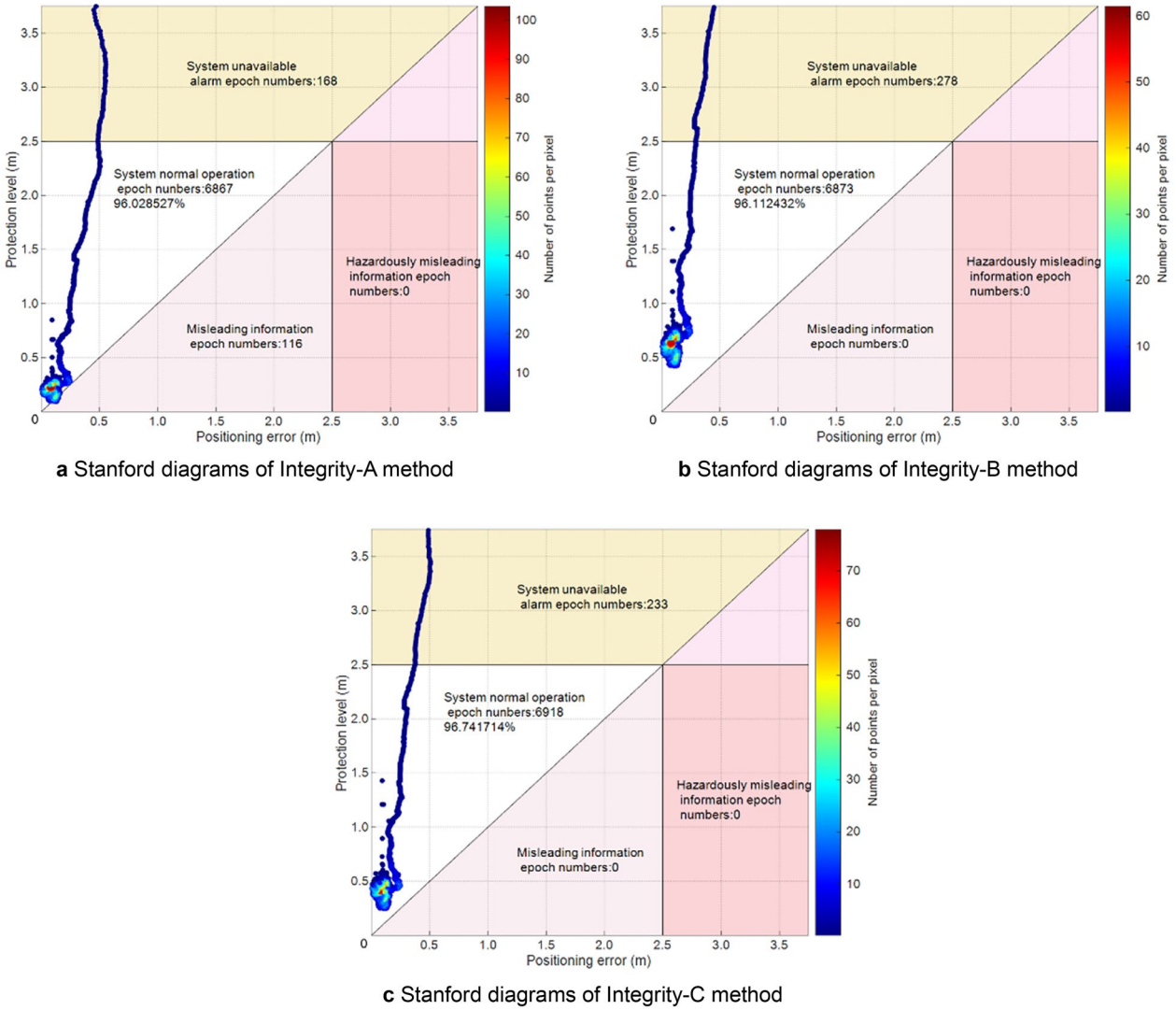


Fig. 9 Stanford diagrams of three methods

Table 8 Receiver system configuration for the ocean experiment

Items	Value/Type
Data type	BDS (B1I/B3I)
	GPS (L1/L2)
Sampling time	00:15 to 04:59 on August 27, 2023, (UTC)
Sampling frequency	1Hz
Receiver type	MA-NP 0101
Antenna type	HX-CSX601A

moving rover being approximately 18 km. The movement trajectory is shown as the green line in Fig. 5. Table 5 describes receiver system configuration for the offshore experiment:

Figure 6 shows HDOP and the number of available satellites for RT-PPP in the offshore experiment. During the experiment, the majority of available satellites are more than 15 and HDOP is within 1, which provides sufficient visible satellites with favorable geometric distribution.

The extracted multipath errors are partitioned into 8 intervals from 10° to 90° with 10° interval. The overbounding of non-Gaussian multipath errors in each interval is performed with the two-step overbounding algorithm, as illustrated in Fig. 7. The blue dots represent the actual multipath errors distribution. The red dots, green dots, and pink dots respectively represent the Gaussian bounds by integrity-A, integrity-B, and integrity-C.

Table 6 lists the specific overbounding coefficients of the two integrity methods. It shows that the

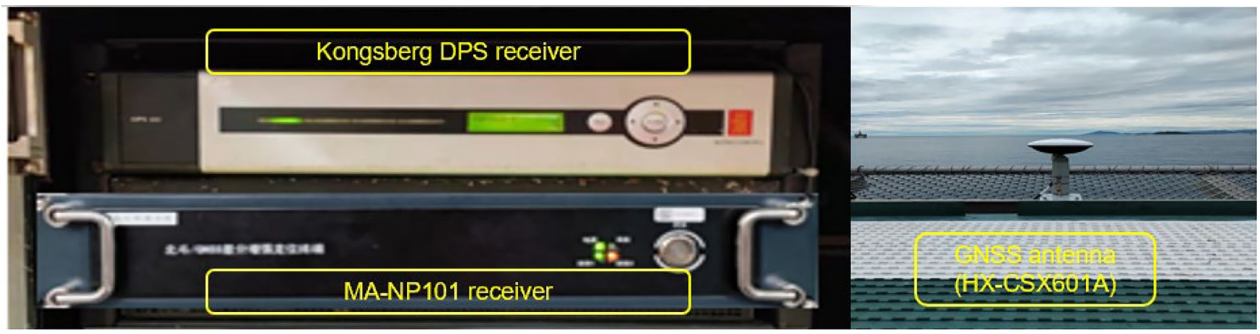


Fig. 10 The experimental equipments

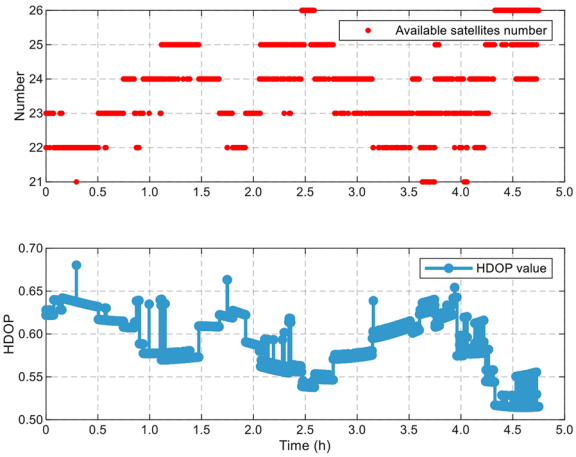


Fig. 11 The available satellite number and HDOP value

overbounding coefficients calculated with the Integrity-C method gradually decrease with increasing elevation angles, while the overbounding coefficients with the Integrity-B are overly conservative for high-elevation satellites. It shows the same characteristics as IGS stations. At approximately 1.2 h in Fig. 6, a temporary drop in the number of visible satellites occurred due to vessel turning, which caused obstruction by the superstructure and the rising/setting of some satellites. This subsequently led to a synchronous and transient rise in the HPL in Fig. 8. This reflects the normal risk response of the integrity monitoring algorithm to the deterioration of in the geometry of available satellite. The event was transient and did not affect the overall system availability; instead, it verified the risk sensitivity and overall robustness of the proposed method in a real dynamic environment.

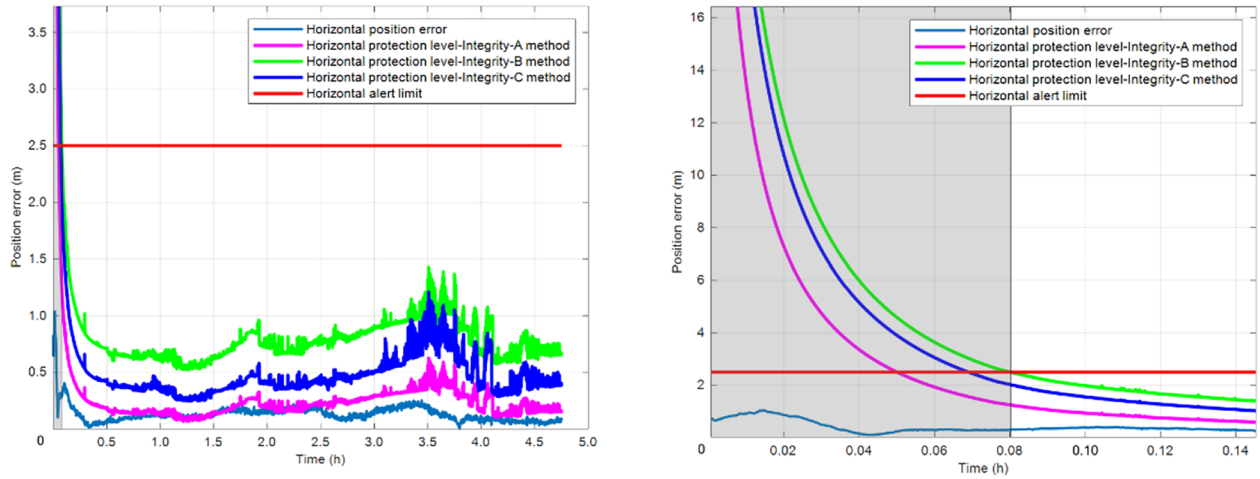
Furthermore, the HPE and MHSS-based PLs with integrity-A, integrity-B, and integrity-C methods are respectively in Fig. 8. Figure 8b presents a detailed view of the initial convergence phase from Fig. 8a, aiming to more clearly illustrate and compare the behavior of the HPL for different integrity monitoring methods during the early convergence period, particularly highlighting the time to first availability. To quantify system availability, the time required for the HPL to converge to the AL is statistically analyzed. The number of epochs required for the Integrity-B method to converge to AL is 278, while that for the Integrity-C method is 233. Compared with Integrity-B, the Integrity-C improves the first availability time by 16.18% with dynamically optimizing overbounding coefficients for different elevation angle intervals.

Table 7 lists the detailed statistical results with the three integrity methods. As shown in Table 7, Integrity-A has the highest detection sensitivity, but contains MI. Integrity-C decreases $R_{H_{\mathrm{HPL}}/E_{\mathrm{HPE}}}$ by 20.45% compared with Integrity-B. Integrity-C makes the HPL closer to the HPE. The HPL calculated with Integrity-B is significantly higher than the HPE due to the overly conservative overbounding model.

To ensure that the proposed approach satisfies the minimum performance requirements defined by the IMO, Fig. 9 shows the Stanford diagrams of the three integrity

Table 9 Comparison of overbounding coefficients

Integrity-B overbounding coefficient	Integrity-C overbounding coefficients in different elevation intervals							
	Elevation intervals 10–20°	Elevation intervals 20–30°	Elevation intervals 30–40°	Elevation intervals 40–50°	Elevation intervals 50–60°	Elevation intervals 60–70°	Elevation intervals 70–80°	Elevation intervals 80–90°
1.40	1.40	1.40	1.35	1.30	1.30	1.26	1.20	1.20



a The HPL of three integrity monitoring methods **b** A detailed view of the initial convergence phase from

Fig. 12 HPL with three integrity monitoring methods in ocean experiment

Table 10 Performance statistics with different methods

Integrity monitoring method	Horizontal protection level (95%)	$R_{H_{\mathrm{HPL}}/E_{\mathrm{HPE}}}$
MHSS-based integrity monitoring with Integrity-A	0.474	2.393
MHSS-based integrity monitoring with Integrity-B	1.179	5.955
MHSS-based integrity monitoring with Integrity-C	0.937	4.730

monitoring algorithms in the offshore experiment. Integrity monitoring performance, including normal operation, unavailability, MI, and HMI, is illustrated by the Stanford diagram. The AL is defined by IMO standards as the maximum allowable HPE in safe operation. It evaluates the integrity performance of the system. The Integrity-A method has a horizontal MI of 1.6%. Both Integrity-B and Integrity-C can effectively suppress MI. At the same time, the normal operation of Integrity-C is more than Integrity-B. Therefore, Integrity-C has improved the system available time.

Ocean experiment

This section evaluates the proposed method in an ocean operation platform approximately 200 km from the coastline. In the ocean experiment scenario, the absence of base stations makes RTK-based reference benchmarks unavailable. Thus, the positioning solutions using a Kongsberg DPS receiver with XP service are employed as the position ground truth, which can achieve positioning accuracy better than 10 cm. The experimental details, parameters settings and experimental equipments are shown in Table 8 and Fig. 10.

Figure 11 shows the number of available satellites and HDOP with the RT-PPP integrity monitoring method in the ocean experiment. In the experiment, HDOP remains below 1.0 and the number of satellites stays above 20.

Table 9 indicates that the overbounding coefficients calculated with the Integrity-C method gradually decrease with increasing elevation angles, while those with the Integrity-B method are overly conservative for high-elevation satellites.

Further, we present the HPE and MHSS-based HPL with integrity-A, integrity-B, and integrity-C methods in Fig. 12. To quantify system availability, the time required for the HPL to converge to the AL is statistically analyzed. The number of epochs required for the Integrity-B method to converge to AL is 288, while that for the Integrity-C method is 248. Compared with Integrity-B, the Integrity-C improves the first availability time by 13.89%.

As shown in Table 10, Integrity-A has the highest detection sensitivity, but contains MI. Integrity-C decreases $R_{H_{\mathrm{HPL}}/E_{\mathrm{HPE}}}$ in the horizontal direction by 20.57% compared with Integrity-B. It makes the HPL closer to the HPE. The HPL calculated with Integrity-B is significantly higher than the HPE due to the overly conservative overbounding model.

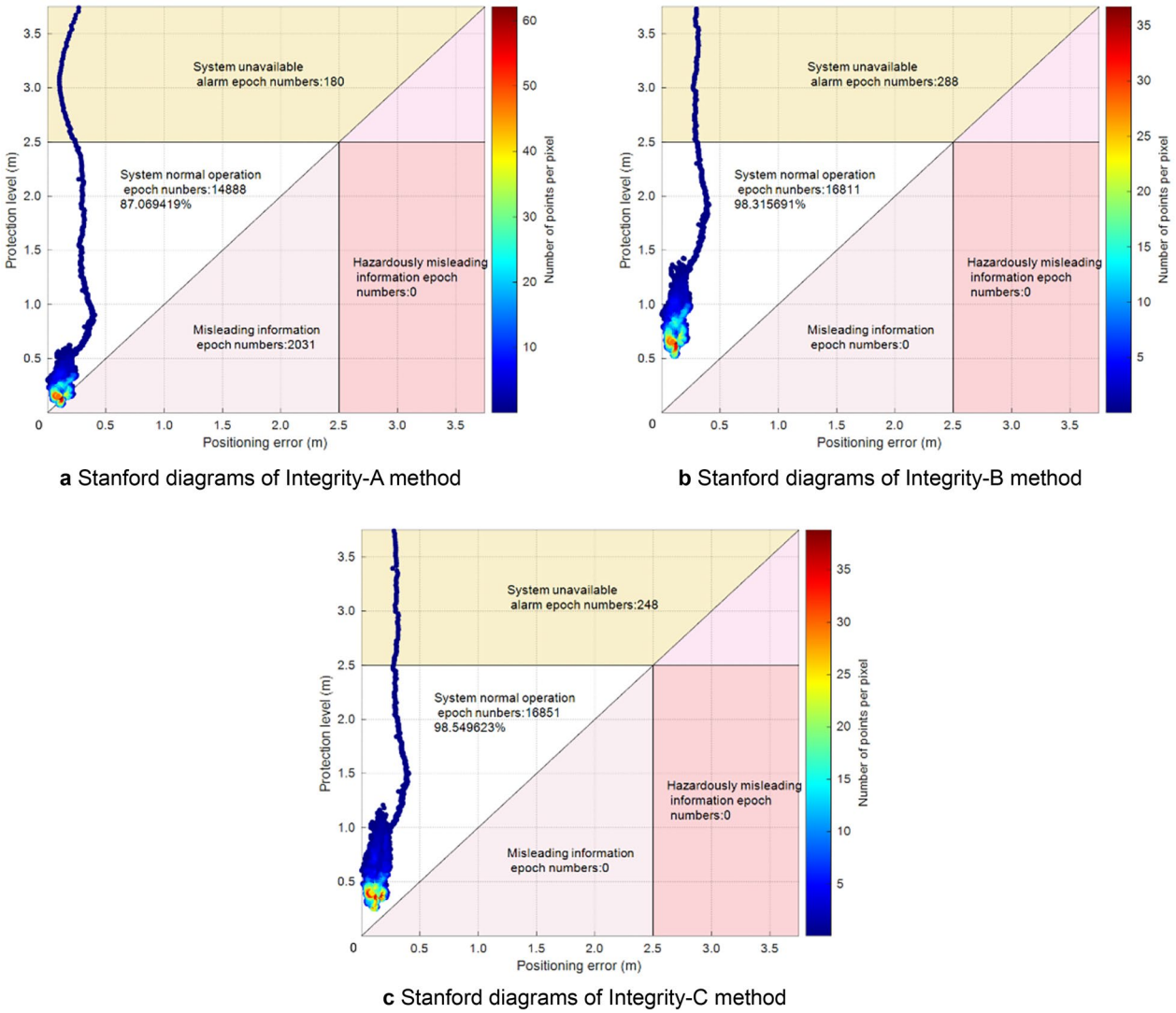


Fig. 13 Stanford diagrams of three methods

Figure 13 shows the Stanford diagrams of the three integrity monitoring algorithms in the open-sea experiment. Integrity-A has a horizontal MI of 11.88%, which does not meet the integrity index requirements of IMO. Both Integrity-B and Integrity-C can effectively suppress MI. At the same time, the normal operation of Integrity-C is more than Integrity-B. Therefore, Integrity-C improves the system available time.

Conclusions

To address the issue of excessively conservative HPL in traditional maritime RT-PPP integrity monitoring, we designed an overbounding method for non-ideal observation errors by considering their elevation-related distribution characteristics. The method extends the two-step overbounding algorithm by incorporating elevation-related error modeling, which better captures non-Gaussian characteristics of maritime multipath errors. It calculates the differentiated overbounding coefficients for distinct satellite elevation intervals. As a refinement of the conventional uniform overbounding approach, it generated HPL that more closely match the HPE while enhancing the availability of the integrity monitoring system. The primary conclusions can be summarized below:

(1) The developed method extends the two-step overbounding algorithm to determine differentiated overbounding coefficients for distinct elevation intervals. By partitioning the multipath errors into

8 intervals and calculating interval-specific overbounding coefficients, the constructed Gaussian bounds better align with actual error multipath distributions.

(2) The theoretical derivation verifies that the proposed overbounding method for RT-PPP integrity monitoring can satisfy the predefined integrity risk requirements, without introducing additional integrity risks. Meanwhile, it is less conservative compared with the traditional two-step overbounding method, which achieves higher availability while meeting the required integrity constraints.

(3) Based on the integrity parameters specified by the IMO, this study conducted real-ship validation of the proposed method in offshore and ocean experiments. Compared to the traditional two-step overbounding algorithm, it generates HPL that more closely match HPE. In offshore experiment, the availability of the proposed method is improved by 16.18%. In ocean experiment, the availability is increased by 11.88%. Both scenarios verified that the method can significantly improve system availability while suppressing misleading information.

It should be noted that the segmentation with 10° elevation interval, while practical, may not fully capture the nuanced behavior of multipath errors across all elevation angles. Additionally, the model is calibrated in typical conditions, and its performance under sustained extreme sea states warrants further validation. Future work will an develop adaptive segmentation method and incorporate real-time environmental data to enhance robustness in dynamic maritime environments.

Acknowledgements
Not applicable.

Author contributions
FY: Writing—original draft, Resources, Methodology; XL: Writing—review & editing, Validation; JZ: Validation, Investigation; WZ: Software, Investigation; LL: Visualization, Supervision, Conceptualization; MQ: Visualization, Conceptualization.

Funding
This research was jointly funded by the National Natural Science Foundation of China (Nos. 62573150, 62373117), the Fundamental Research Funds for Central Universities (No. 3072025GH0401), China Postdoctoral Science Foundation (Nos. No.2024M754064, 2023M730831).

Data availability
The data generated and/or analyzed during the current study are not publicly available for legal/ethical reasons but are available from the corresponding author on reasonable request.

Declarations

Competing interests
The authors declare that they have no known competing financial interests or personal relationships that could have appeared to influence the work reported in this paper.

Received: 19 October 2025 Revised: 2 February 2026 Accepted: 2 February 2026
Published online: 11 March 2026

References

Ashby, N. (2003). Relativity in the global positioning system. *Living Reviews in Relativity, 6*(1), 1–42. https://doi.org/10.12942/lrr-2003-1

Bevis, M., Businger, S., Herring, T. A., Rocken, C., Anthes, R. A., & Ware, R. H. (1992). GPS meteorology: Remote sensing of atmospheric water vapor using the global positioning system. *Journal of Geophysical Research: Atmospheres, 97*(D14), 15787–15801. https://doi.org/10.1029/92jd01517

Blanch, J., Gunning, K., Walter, T., De Groot, L., & Norman, L. (2019). Reducing computational load in solution separation for Kalman filters and an application to PPP integrity. In: *Proceedings of the 2019 International Technical Meeting of The Institute of Navigation* (pp. 720–729). https://doi.org/10.33012/2019.16721

Blanch, J., Walter, T., & Enge, P. (2018). Gaussian bounds of sample distributions for integrity analysis. *IEEE Transactions on Aerospace and Electronic Systems, 55*(4), 1806–1815. https://doi.org/10.1109/TAES.2018.2876583

Chen, L., Song, W., Yi, W., Shi, C., Lou, Y., & Guo, H. (2017). Research on a method of real-time combination of precise GPS clock corrections. *GPS Solutions, 21*(1), 187–195. https://doi.org/10.1007/s10291-016-0515-3

DeCleene, B. (2000). Defining pseudorange integrity-overbounding. *In: Proceedings of the 13th international technical meeting of the satellite division of the institute of navigation (ION GPS 2000)* (pp. 1916–1924).

Geng, J., Teferle, F. N., Meng, X., & Dodson, A. H. (2010). Kinematic precise point positioning at remote marine platforms. *GPS Solutions, 14*(4), 343–350. https://doi.org/10.1007/s10291-009-0157-9

Geng, T., Cheng, L., Xie, X., Liu, J., Li, Z., & Jiang, R. (2022a). GNSS real-time precise point positioning with BDS-3 global short message communication devices. *Advances in Space Research, 70*(3), 576–586. https://doi.org/10.1016/j.asr.2022.04.068

Geng, T., Ma, Z., Xie, X., Tao, J., Liu, T., Zhao, Q., & Li, J. (2022b). Multi-GNSS real-time precise point positioning using BDS-3 global short-message communication to broadcast corrections. *GPS Solutions, 26*(3), 99. https://doi.org/10.1007/s10291-022-01284-6

Gunning, K., Blanch, J., Walter, T., De Groot, L., & Norman, L. (2018). Design and evaluation of integrity algorithms for PPP in kinematic applications. In: *Proceedings of the 31st International Technical Meeting of the Satellite Division of The Institute of Navigation (ION GNSS+ 2018)* (pp. 1910–1939). https://doi.org/10.33012/2018.15972

He, Z., Zhang, S., Nan, Y., Liu, K., Qu, W., Wu, H., & Liu, Q. (2018). Analysis of sea surface multipath and impact on GNSS precision positioning. In: *China Satellite Navigation Conference* (pp. 173–185). Singapore: Springer Singapore. https://doi.org/10.1007/978-981-13-0005-9_15

Heßelbarth, A., & Wanninger, L. (2013). SBAS orbit and satellite clock corrections for precise point positioning. *GPS Solutions, 17*(4), 465–473. https://doi.org/10.1007/s10291-012-0292-6

IMO Resolution A. (2002) 915(22), Revised maritime policy and requirements for a future GNSS. London.

IMO Resolution A. (2004) 953(23), Revised world-wide radionavigation system. London.

Kouba, J. (2009). A guide to using international GNSS service (IGS) products. https://files.igs.org/pub/resource/pubs/UsingIGSProductsVer21_cor.pdf

Li, L., Li, Z., Yuan, H., Wang, L., & Hou, Y. (2016). Integrity monitoring-based ratio test for GNSS integer ambiguity validation. *GPS Solutions, 20*(3), 573–585. https://doi.org/10.1007/s10291-015-0468-y

Liu, R., & Jiang, Y. (2024). Overbounding multipath error in urban canyon with LSTM using multi-sensor features. *IEEE Transactions on Intelligent*

Transportation Systems, 25(9), 10926–10940. https://doi.org/10.1109/tits.2024.3376812
Zishen, W., & Ningbo, L. I. (2023). *Basic Framework of BDS-based High-precision and High-credibility PPP-RTK Service. Navigation Positioning and Timing*. 10, 7–15.
Long, C., Wu, Z., & Shen, Z. (2023). UWB enhanced GNSS precise point positioning based on raw measurements. *Navigation Positioning and Timing, 10*(4), 123–131.
Mervart, L., & Weber, G. (2011). Real-time combination of GNSS orbit and clock correction streams using a Kalman filter approach. In: *Proceedings of the 24th International Technical Meeting of The Satellite Division of the Institute of Navigation (ION GNSS 2011)* (pp. 707–711).
Rife, J., Pullen, S., Enge, P., & Pervan, B. (2006). Paired overbounding for nonideal LAAS and WAAS error distributions. *IEEE Transactions on Aerospace and Electronic Systems, 42*(4), 1386–1395. https://doi.org/10.1109/TAES.2006.314579
Seepersad, G., & Bisnath, S. (2015). Reduction of PPP convergence period through pseudorange multipath and noise mitigation. *GPS Solutions, 19*(3), 369–379. https://doi.org/10.1007/s10291-014-0395-3
Sirisha, V., Srinivas, V. S., & Rajini, P. (2019). Statistical modelling of GNSS multipath error using triple-frequency linear combination. In: *2019 URSI Asia-Pacific Radio Science Conference (AP-RASC)* (pp. 1–3). IEEE. https://doi.org/10.23919/ursiap-rasc.2019.8738287
Wang, E., Yu, T., Sun, X., Qu, P., Chen, T., Hong, X., Xu, S., & Liu, Z. (2025a). A GNSS PPP integrity monitoring algorithm based on ARKF and MHSS. *Advances in Space Research, 75*(10), 7397–7406. https://doi.org/10.1016/j.asr.2025.03.004
WANG, L., LI, L., CHEN, L., WANG, N., LI, Z., MA, W., ... & LIU, X. (2025). Preliminary performance evaluation of integrity service for real-time precise satellite orbit and clock. *Geomatics and Information Science of Wuhan University*. https://doi.org/10.13203/J.whugis20240396
Wang, S., Zhan, X., Xiao, Y., & Zhai, Y. (2022). Integrity monitoring of PPP-RTK based on multiple hypothesis solution separation. In: *China Satellite Navigation Conference* (pp. 321–331). Singapore: Springer Nature Singapore. https://doi.org/10.1007/978-981-19-2580-1_27
Weinbach, U., Brandl, M., Chen, X., Landau, H., Pastor, F., Reussner, N., & Rodriguez-Solano, C. (2018). Integrity of the trimble® centerpoint RTX correction service. In: *proceedings of the 31st international technical meeting of the satellite division of the institute of navigation (ION GNSS+ 2018)* (pp. 1902–1909).
Wu, J. T., Wu, S. C., Hajj, G. A., Bertiger, W. I., & Lichten, S. M. (1992). Effects of antenna orientation on GPS carrier phase. *Astrodynamics, 1991*, 1647–1660. https://doi.org/10.1007/BF03655303
Xiao, Y., Zhan, X., Wang, S., & Zhai, Y. (2025). Ensuring high integrity of GNSS precise orbit and clock products based on performance-assured sliding-window innovation test. *Advances in Space Research, 75*(4), 3340–3349. https://doi.org/10.1016/j.asr.2024.12.003
Yang, F., Zhao, L., Li, L., Feng, S., & Cheng, J. (2019). Performance evaluation of kinematic BDS/GNSS real-time Precise Point Positioning for maritime positioning. Journal of Navigation, 72(1), 34–52. https://doi.org/10.1017/s0373463318000644
Zhang, J., Yang, F., Li, J., Hu, P., Liu, X., & Zhao, L. (2024). State-domain based integrity monitoring of satellite orbit and clock corrections for RT-PPP. *IEEE Sensors Journal*, 25 (2), 3061-3073. https://doi.org/10.1109/JSEN.2024.3504408
Zhang, J., Yang, F., Li, J., Sun, Z., Zhang, R., & Zhao, L. (2025). Integrity monitoring for real-time precise point positioning in maritime precise operating environment. *Measurement, 253*, 117574. https://doi.org/10.1016/j.measurement.2025.117574
Zhang, J., Zhao, L., Yang, F., Li, L., Liu, X., & Zhang, R. (2022). Integrity monitoring for undifferenced and uncombined PPP under local environmental conditions. *Measurement Science and Technology, 33*(6), 065010. https://doi.org/10.1088/1361-6501/ac4b12
Zhao, L., Yang, F., Li, L., Ding, J., & Zhao, Y. (2016). GBAS ionospheric anomaly monitoring based on a two-step approach. *Sensors, 16*(6), 763. https://doi.org/10.3390/s16060763
Zumberge, J. F., Heflin, M. B., Jefferson, D. C., Watkins, M. M., & Webb, F. H. (1997). Precise point positioning for the efficient and robust analysis of GPS data from large networks. *Journal of Geophysical Research: Solid Earth, 102*(B3), 5005–5017. https://doi.org/10.1029/96JB03860

Publisher's Note

Springer Nature remains neutral with regard to jurisdictional claims in published maps and institutional affiliations.